Supporting Information

Interlocking Friction Governs the Mechanical Fracture of Bilayer MoS_2

Gang Seob Jung[1*], Shanshan Wang[2*], Zhao Qin[1], Francisco J. Martin-Martinez[1], Jamie H. Warner[2†] & Markus J. Buehler[1,3†]

[1] Laboratory for Atomistic and Molecular Mechanics (LAMM), Department of Civil and Environmental Engineering, Massachusetts Institute of Technology, 77 Massachusetts Ave., Cambridge 02139, MA, USA

[2]Department of Materials, University of Oxford, Parks Road, Oxford, OX1 3PH, United Kingdom

[3]Center for Computational Engineering, Massachusetts Institute of Technology, 77 Massachusetts Ave., Cambridge, MA 02139, USA

†Email: (jamie.warner@materials.ox.ac.uk) or (mbuehler@mit.edu).
*These authors contributed equally to this work

1. DFT calculation for binding energy of MoS_2 bilayer

Lennard-Jones (LJ) parameters of Reactive Empirical Bond Order (REBO) force field (FF)[1-3] were tuned for van der Waals (vdW) interaction of MoS_2 bilayers from our Density Functional Theory (DFT) calculations by Quantum-Espresso package[4] using Perdew Burke Ernzerhof (PBE) functional[5] and norm-conserving type pseudopotential.[6] Grimme's DFT-D2 correction was applied for vdW interaction between the two layers.[7] A hexagonal unit cell for DFT calculation contains 6 atoms with the periodic boundary condition in *a* and *b* directions as shown in Figure S1a. The energy cutoff for the wave functions was 60 Ry and 11×11×1 Monkhost-Pack grids were adopted for the K space sampling. The formation energy ($E_{form} = E_{bilayer} - 2E_{monolayer}$) per atom as a function of the interlayer distance (h) was obtained by structural relaxation, ranging from 5.5 Å to 9 Å with 0.1 Å spacing in Figure S1b. To model the 2D system, 32 Å vacuum was inserted to avoid undesirable interaction between periodic images. The vacuum space allowed more than 15 Å between layers, which is enough to ignore the interaction from the periodic images. Our calculations of the equilibrium interlayer distance (h_{equil}) and the binding energy ($E_b = -E_{form}$) for AA'(2H), AB(3R), and AA stacks show good agreement with previous studies,[8,9] as shown in Table S1 and S2. There are mainly two different types of interlayer interactions. Type I, AA'(2H) and AB(3R), has high binding energy with shorter equilibrium distance than Type II, AA, as shown in Figure S1. The difference between the two types is the key to describe the interaction of bilayer MoS_2, which is not captured in the original FF as shown in Figure S1b. Thus, the LJ parameters were optimized mainly based on the energy profiles of AA'(2H) and AA from DFT calculations.

2. Parameter optimization for vdW binding energy (REBO*)*

Molecular Dynamics (MD) simulations in this study were performed *via* a LAMMPS MD package.[10] To evaluate the binding energy, a rectangular unit cell was prepared containing 12 atoms with periodic boundary conditions in both *x* and *y* directions as shown in Figure S1a. The system has enough vacuum space (more than 30 Å) for the same reason that we inserted vacuum in the DFT calculations to avoid the interaction between periodic images. The LJ parameters were obtained to match the formation energy profiles from MD to those from DFT. Table S3 shows the LJ parameters used in the current study. The parameters for Mo-S interaction, σ_{MS} and $\varepsilon_{MS,}$ were explicitly applied for Mo-S interaction instead of the conventional mixing rules used in the original form. Also, the shorter radius cutoff, $r_{cutMS} \sim 1.5\ \sigma_{MS}$ was applied (originally $r_{cutMS} = 2.5\ \sigma_{MS}$). This shorter r_{cutMS} is helpful to describe the difference between the two stacks while too short r_{cutMS} results in non-continuous formation energy profiles. The formation energy profiles from the original and optimized FFs are shown in Figure S1b, which shows significant improvement for the layer-to-layer interaction.

3. Parameter optimization for mechanical properties of monolayer MoS_2 (REBO)

The optimized LJ parameters slightly affected the mechanical properties of MoS_2 monolayer. Thus, tuning other parameters related to covalent bonds was required after modification of LJ parameters. We utilized the stress-strain curves from the previous DFT calculations and applied the same strategy to tune the parameters.[11,12] Firstly, we fitted the failure points of stress-strain curves of MD to DFT results by adjusting radius cutoffs of switching functions. We completely turned off the switching function by setting $R_{min} = R_{max}$ for Mo-S interaction as utilized in the REBO for hydrocarbon system,[13,14] which is very important to describe realistic bond breaking and forming without nonphysical stiffening. For the stress-strain curves of MoS_2 monolayer with MD simulation, MoS_2 monolayer with 5 nm x 5 nm was prepared to perform tensile tests in both the zigzag (ZZ) and armchair (AC) directions under a plane strain condition and the periodic boundary condition. The strain rate was set to 0.2 Å/ps (20m/s) for dynamics loadings with NVT ensemble with a low temperature (~10K) to ignore temperature effects. Then, we rescaled the attractive and repulsive terms[2,3] to fit the stiffness of MD to that of DFT. The parameters tuned by this process could successfully describe the experimental observation of MoS_2 monolayer crack propagation with vacancies of sulfurs.[11] Next, the elastic constants (C_{11}, C_{12}, C_{22}) were obtained by calculating the stresses with 0.5% strains in both DFT and MD calculations. The previous DFT/MD calculation,[15] and experiment[16] used the unit, N/m, for strength and stiffness to ignore the uncertainty of the thickness of MoS_2. The reported stiffness and strength[16] of monolayer MoS_2 from nano-indentation were 180 ± 60 N/m and 15±3 N/m, respectively. The values show good agreement with the mechanical properties obtained from our DFT calculations. As shown in Figure S2 and Table S4, the mechanical properties and geometric parameters from our MD simulations show good agreement with those from DFT calculations

4. Crack blocking: Crack propagation into stacked finite bilayer regions

We prepared a 30x50nm rectangular MoS_2 layer (bottom layer) for the crack region with a circular layer (top layer) with a 14nm radius for the uncracked region as shown in Figure S4a. The circular regions were stacked in six different ways: 0º (3R), 15º, 30º, 45º, and 60º (2H) rotated. In the beginning, the systems were stretched with 3.2% tensile strain in the *x* direction, which allowed crack propagation and broke the monolayer layer as shown in Figure S4b. After energy minimization, the system was relaxed with NVT ensemble at low temperature 10K for 100ps with 1fs time step. At this point, the bottom layer was still pre-stretched but the top layer was fully relaxed without rotation. Then, NVE ensemble was applied to ignore the undesired effects from the thermostat before a crack insertion in the bottom layer. After a sharp crack (l_c = 15nm) was inserted in the bottom layer and the crack propagation was observed as shown in Figure S4b.

5. Coherent fracture: Crack propagation into stacked semi-infinite bilayer regions

Instead of a finite circular layer, a semi-infinite top layer that is large enough to be pre-stretched with the bottom layer was modeled. A square layer (30 x 30 nm) was stacked on the bottom layer with different angles: 0º (3R), 15º, and 60º (2H). The bottom layer was 30 x 40nm and the entire system was relaxed with NVT ensemble at 10K for 100ps after energy minimization. The ensemble was changed from NVT to NVE and the major crack (l_c = 8nm) in the bottom layer was inserted. Different flaws were introduced in the top layer from 0 to 3nm crack (l_{c2}) on the crack-path in the bottom layer as shown in Figure S6a. The flaw lengths were too short to allow the crack propagation in the top layer with the applied pre-strain (~5%).

6. Crack branching: Cracks in 2H stacked bilayer MoS_2

From the experimental observation in Figure 5, we prepared the 40 x 40nm square layer for the top and bottom layer with 2H-stacked condition as shown in Figure S7a. First, different ratios of defects were introduced in the defect region of the top layer where the width is 2nm and the length is 40nm. Each model was relaxed with 4% pre-strain in the *x* direction. After energy minimization, the system was relaxed with NVT ensemble at 10K for 100ps. The ensemble was changed from NVT to NVE and a crack (lc ~8nm) was introduced in the bottom layer. The stored strain energy allowed the crack start to propagate, and the natural behaviors of both layers were observed. The left and right boundaries were fixed in the *x* direction and top and bottom boundaries were fixed in the *y* direction with a non-periodic boundary condition, mimicking the main features from the experimental structure in Figure 5.

Supporting Table 1. The binding energy obtained from DFT calculation with Grimme's vdW-D2 correction and MD with both original and optimized reactive FFs. The difference of the binding energy between 2H and 3R are improved.

E_b (meV/atom)	AA	AA' (2H)	AB (3R)
DFT-D2	14.1	24.1	23.8
Original FF	11.6	16.2	16.3
Optimized FF	15.6	22.0	21.7

Supporting Table 2. The equilibrium distance obtained from DFT calculation with Grimme's vdW-D2 correction and MD with both original and optimized reactive FFs. The difference of the equilibrium distance between 2H and 3R are improved.

h_{equil} (Å)	AA	AA' (2H)	AB (3R)
DFT-D2	6.7	6.2	6.3
Original FF	6.5	6.1	6.1
Optimized FF	6.7	6.3	6.3

Supporting Table 3. The original and optimized Lennard-Jones parameters for the layer-to-layer interaction. Explicit parameters for σ_{MS} and ε_{MS} are utilized instead of conventional mixing rules.

LJ parameters	σ_{MM} (Å)	σ_{MS} (Å)	σ_{SS} (Å)	ε_{MM} (eV)	ε_{MS} (eV)	ε_{SS} (eV)
Original FF	4.2	3.665	3.13	0.00058595	0.0028498	0.01386
Optimized FF	3.6	3.165	3.25	0.00093752	0.00455965	0.022176

Supporting Table 4. The geometric parameters and elastic constant of monolayer MoS_2 from DFT calculations and MD.

	Original FF	Optimized FF (current study)	DFT (current study)	DFT[15] (reference)
Mo-Mo (S-S)	3.17	3.21	3.18	3.18
Mo-S	2.44	2.46	2.45	2.41
$t(S_{top}\text{-}S_{bottom})$	3.24	3.24	3.20	3.11
C_{11} (N/m)	149.0	127.9	129.9	123.3
C_{12} (N/m)	41.9	38.5	29.3	32.9
C_{22} (N/m)	149.0	127.9	130.2	124.3
E (N/m)	137.0	116.3	123.5	114.5

Supporting Table 5. Friction forces per area in the +ZZ direction for the rotational stacking from 2H stack: θ = 0º (3R) 15º, 30º, 45º, 60º (2H) with four different sizes: 2R = 5, 7, 10, 15nm.

2R	0º (3R or AB)	15º	30º	45º	60º (2H or AA')
5 nm	0.38	0.081	0.068	0.076	0.41
7 nm	0.41	0.071	0.066	0.063	0.36
10 nm	0.34	0.069	0.060	0.032	0.32
15 nm	0.30	0.063	0.061	0.032	0.28
Avg (nN/nm^2)	0.37 ± 0.04	0.071 ± 0.008	0.064 ± 0.003	0.065 ± 0.004	0.34 ± 0.06

Supporting Table 6. Friction forces per area in the -ZZ direction for the rotational stacking from 2H stack: θ = 0º (3R) 15º, 30º, 45º, 60º (2H) with four different sizes: 2R = 5, 7, 10, 15nm.

2R	0º (3R or AB)	15º	30º	45º	60º (2H or AA')
5 nm	0.34	0.049	0.054	0.051	0.37
7 nm	0.35	0.057	0.060	0.055	0.37
10 nm	0.32	0.056	0.054	0.058	0.34
15 nm	0.29	0.057	0.056	0.061	0.31
Avg (nN/nm^2)	0.33 ± 0.03	0.055 ± 0.003	0.056 ± 0.003	0.056 ± 0.005	0.35 ± 0.03

Supporting Table 7. Friction forces per area in the +AC direction for the rotational stacking from 2H stack: θ = 0º (3R) 15º, 30º, 45º, 60º (2H) with four different sizes: 2R = 5, 7, 10, 15nm. For 2H and 3R, two peak forces are recorded.

2R	0º (3R or AB)	15º	30º	45º	60º (2H or AA')
5 nm	0.50 / 0.15	0.060	0.059	0.065	0.26 / 0.52
7 nm	0.54 / 0.16	0.055	0.055	0.058	0.24 / 0.57
10 nm	0.53 / 0.15	0.056	0.055	0.060	0.24 / 0.52
15 nm	0.48 / 0.13	0.054	0.060	0.058	0.23 / 0.47
Avg (nN/nm^2)	0.52 ± 0.03 0.15 ± 0.01	0.056 ± 0.003	0.057 ± 0.003	0.060 ± 0.003	0.24 ± 0.01 0.52 ± 0.04

Supporting Table 8. Friction forces per area in the -AC direction for the rotational stacking from 2H stack: θ = 0º (3R) 15º, 30º, 45º, 60º (2H) with four different sizes: 2R = 5, 7, 10, 15nm. For 2H and 3R, two peak forces are recorded.

2R	0º (3R or AB)	15º	30º	45º	60º (2H or AA')
5 nm	0.27 / 0.54	0.066	0.064	0.066	0.53 / 0.11
7 nm	0.25 / 0.53	0.071	0.062	0.066	0.59 / 0.15
10 nm	0.23 / 0.51	0.066	0.066	0.064	0.52 / 0.14
15 nm	0.25 / 0.48	0.064	0.063	0.064	0.50/ 0.14
Avg (nN/nm^2)	0.25 ± 0.01 0.52 ± 0.03	0.067 ± 0.003	0.064 ± 0.002	0.065± 0.002	0.53 ± 0.04 0.14 ± 0.02

7. SI References

(1) Brenner, D. W.; Shenderova, O. A.; Harrison, J. A.; Stuart, S. J.; Ni, B.; Sinnott, S. B., A Second-Generation Reactive Empirical Bond Order (REBO) Potential Energy Expression for Hydrocarbons. *J. Phys.: Condens. Matter* **2002**, *14*, 783-802.

(2) Liang, T.; Phillpot, S. R.; Sinnott, S. B., Parametrization of a Reactive Many-Body Potential for Mo–S Systems. *Phys. Rev. B* **2009**, *79*, 245110-14.

(3) Stewart, J. A.; Spearot, D. E., Atomistic Simulations of Nanoindentation on the Basal Plane of Crystalline Molybdenum Disulfide (MoS_2). *Modell. Simul. Mater. Sci. Eng.* **2013**, *21*, 045003-15.

(4) Giannozzi, P.; Baroni, S.; Bonini, N.; Calandra, M.; Car, R.; Cavazzoni, C.; Ceresoli, D.; Chiarotti, G. L.; Cococcioni, M.; Dabo, I.; Corso, A. D.; de Gironcoli, S.; Fabris, S.; Fratesi, G.; Gebauer, R.; Gerstmann, U.; Gougoussis, C.; Kokalj, A.; Lazzeri, M.; Martin-Samos, L.*, et al.*, QUANTUM ESPRESSO: a Modular and Open-Source Software Project for Quantum Simulations of Materials. *J. Phys.: Condens. Matter* **2009**, *21*, 395502.

(5) Perdew, J. P.; Burke, K.; Ernzerhof, M., Generalized Gradient Approximation Made Simple. *Phys. Rev. Lett.* **1996**, *77*, 3865-3868.

(6) Troullier, N.; Martins, J. L., Efficient Pseudopotentials for Plane-Wave Calculations. *Phys. Rev. B* **1991,** *43*, 1993-2006.

(7) Grimme, S., Semiempirical GGA-Type Density Functional Constructed with a Long-Range Dispersion Correction. *J. Comput. Chem.* **2006**, *27*, 1787-1799.

(8) He, J.; Hummer, K.; Franchini, C., Stacking Effects on the Electronic and Optical Properties of Bilayer Transition Metal Dichalcogenides MoS_2, $MoSe_2$, WS_2, and WSe_2. *Phys. Rev. B* **2014**, *89*, 075409-11.

(9) Tao, P.; Guo, H.-H.; Yang, T.; Zhang, Z.-D., Stacking Stability of MoS_2 Bilayer: An *Ab Initio* Study. *Chinese Physics B* **2014**, *23*, 106801-6.

(10) Plimpton, S., Fast Parallel Algorithms for Short-Range Molecular Dynamics. *J. Comput. Phys.* **1995**, *117*, 1-19.

(11) Wang, S.; Qin, Z.; Jung, G. S.; Martin-Martinez, F. J.; Zhang, K.; Buehler, M. J.; Warner, J. H., Atomically Sharp Crack Tips in Monolayer MoS2 and Their Enhanced Toughness by Vacancy Defects. *ACS Nano* **2016**, *10*, 9831-9839.

(12) Han, Y.; Li, M.-Y.; Jung, G.-S.; Marsalis, M. A.; Qin, Z.; Buehler, M. J.; Li, L.-J.; Muller, D. A., Sub-Nanometre Channels Embedded in Two-Dimensional Materials. *Nat. Mater.* **2017**, *17*, 129-133.
(13) Qin, Z.; Jung, G. S.; Kang, M. J.; Buehler, M. J., The Mechanics and Design of a Lightweight Three-Dimensional Graphene Assembly. *Sci. Adv.* **2017**, *3*, e1601536.
(14) Jung, G. S.; Yeo, J.; Tian, Z.; Qin, Z.; Buehler, M. J., Unusually Low and Density-Insensitive Thermal Conductivity of Three-Dimensional Gyroid Graphene. *Nanoscale* **2017**, *9*, 13477-13484.
(15) Xiong, S.; Cao, G., Molecular Dynamics Simulations of Mechanical Properties of Monolayer MoS_2. *Nanotechnology* **2015**, *26*, 1-11.
(16) Bertolazzi, S.; Brivio, J.; Kis, A., Stretching and Breaking of Ultrathin MoS_2. *ACS Nano* **2011**, *5*, 9703-9709.

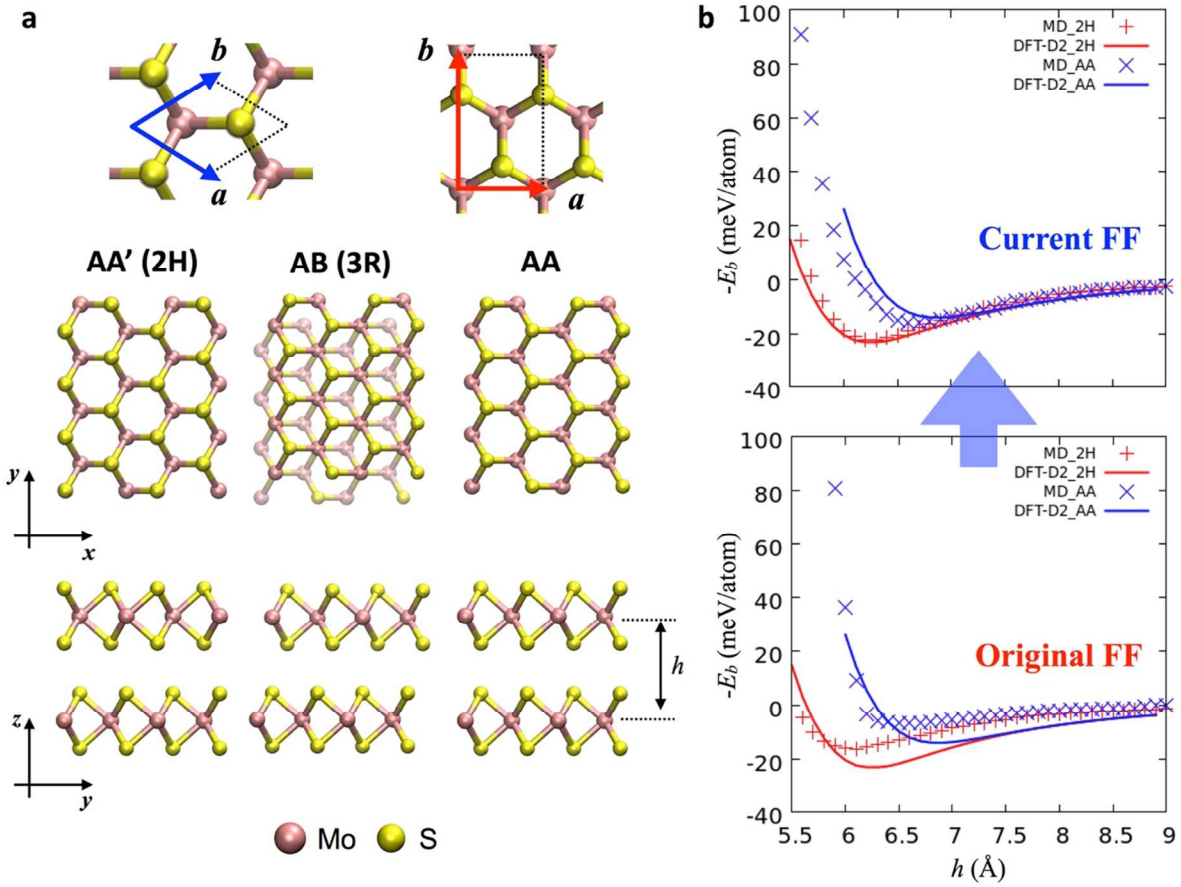

Figure S1. (**a**) Three representative stacking geometries of MoS_2 bilayer. (**b**) Formation energy profiles comparison between original FF and current FF, showing DFT and MD results for binding energy of bilayer MoS_2 as a function of the interlayer distance (h).

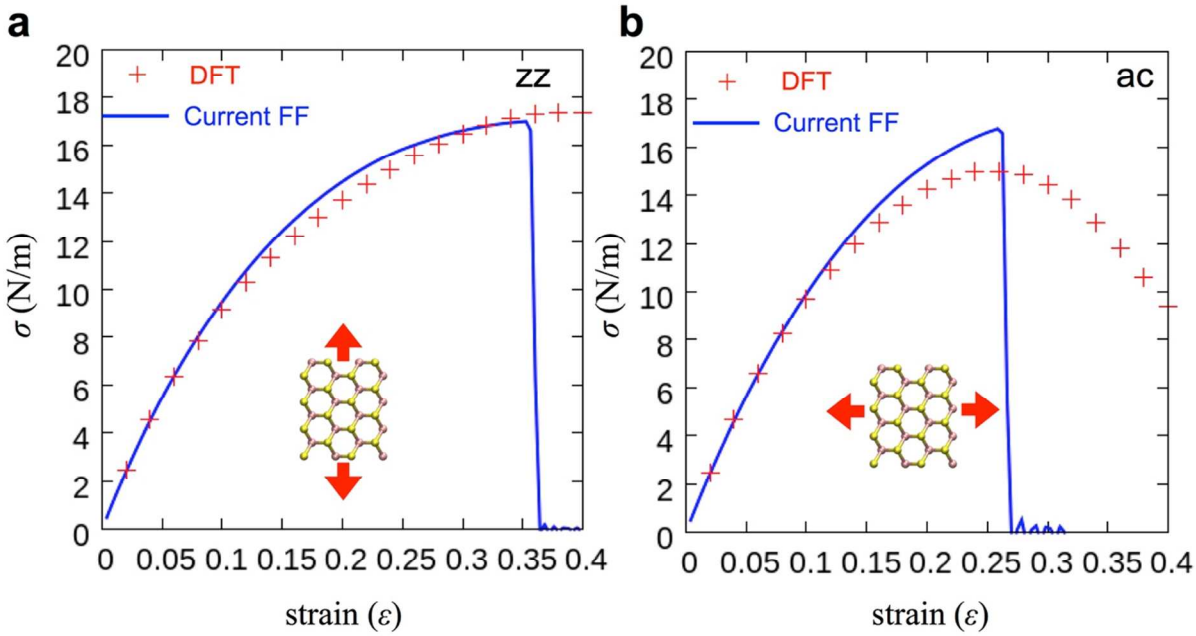

Figure S2. The stress-strain curves under the uniaxial tensile loadings in the zigzag (**a**) and armchair directions (**b**) with a plane strain condition. The failure strain and strength from the current REBO are well matched with those from DFT calculations. The stress unit (N/m) is used to ignore the uncertainty of the thickness of MoS_2 as the previous experimental and theoretical studies used.[15,16]

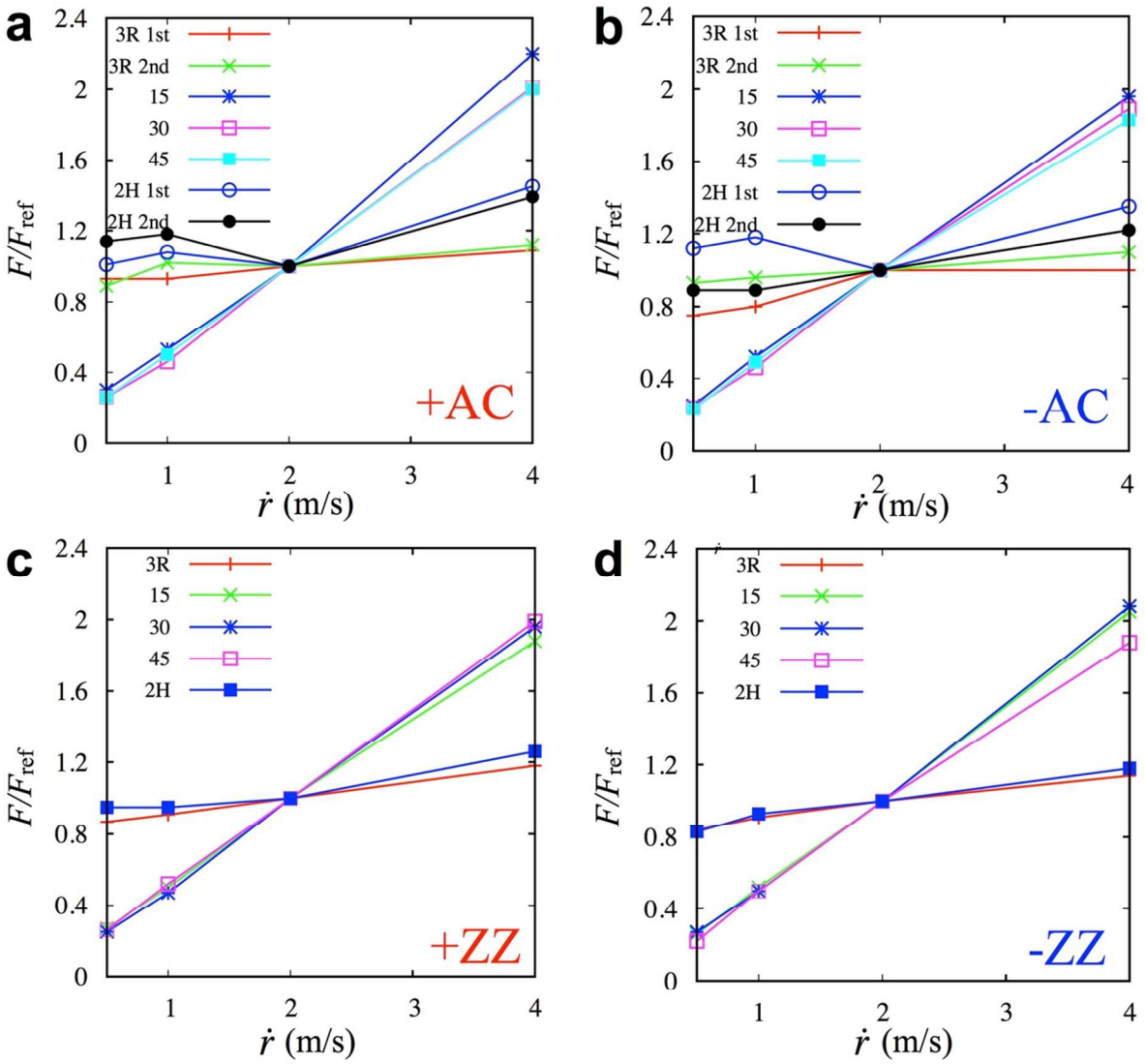

Figure S3. Strain effects on frictions. The normalized factors are shown with the different loading rates of +AC, -AC, +ZZ and –ZZ for (**a-d**) The frictions of turbostratic stacks show a linear relation with the loading rates while the frictions of 2H and 3R are less sensitive to the loading rate slower than 0.02Å/ps (2m/s).

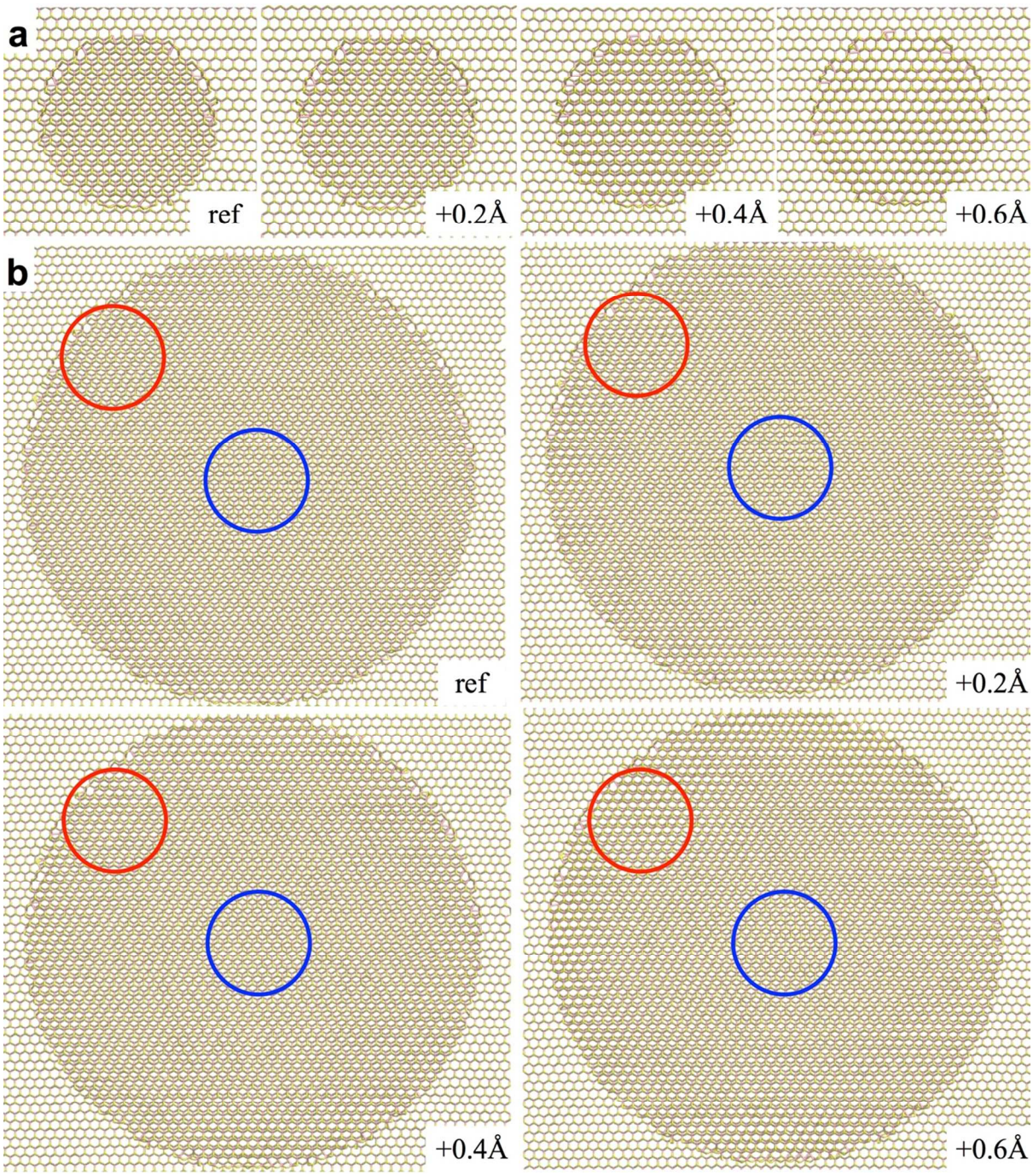

Figure S4. Snap shots of the friction test in the +AC direction in Figure 2a with *R*=50Å(**a**) and 150Å(**b**). As the size of the radius increases, the friction is likely to decrease by utilizing local deformation. The two circles indicate the locally different geometries between the two regions during the loading.

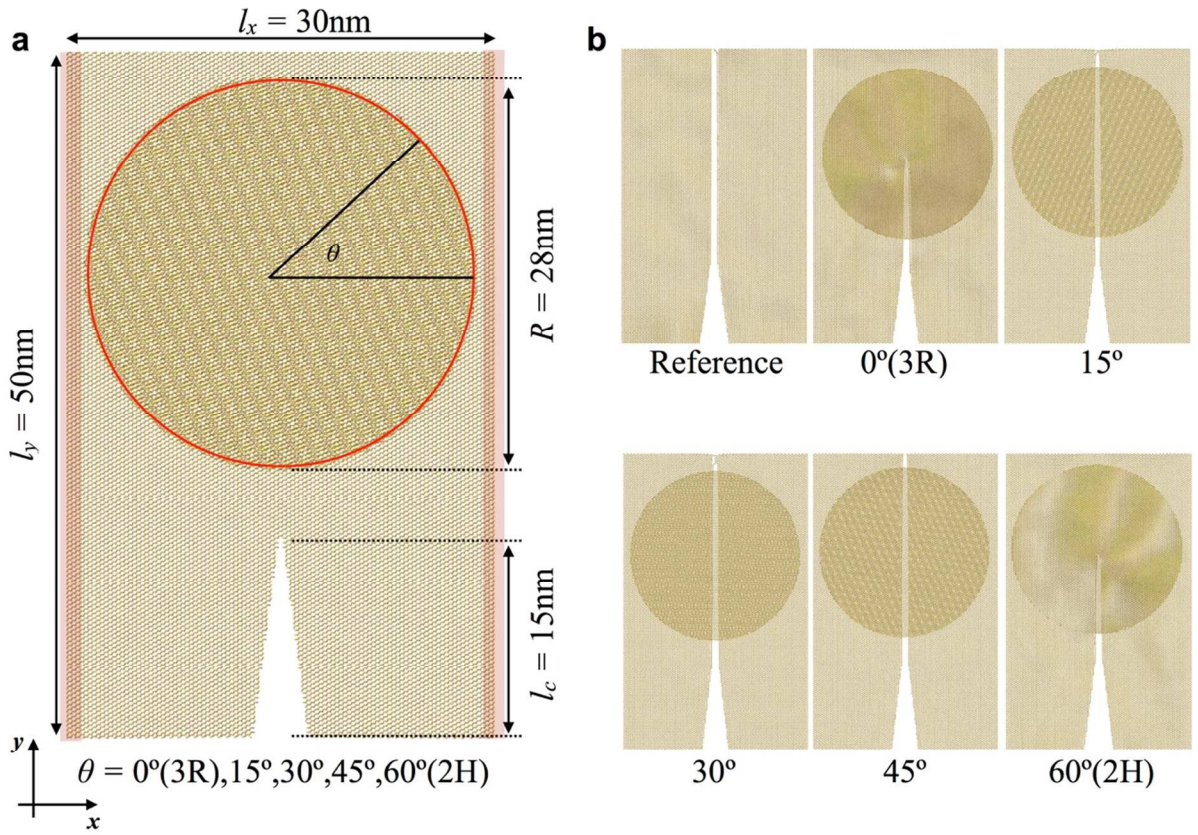

Figure S5. (**a**) Schematic figure for crack propagation into bilayer region. (**b**) Results of crack propagations. The stack conditions significantly affect the crack-tip propagation. Only 2H and 3R stacks show that the crack propagation is disturbed and blocked.

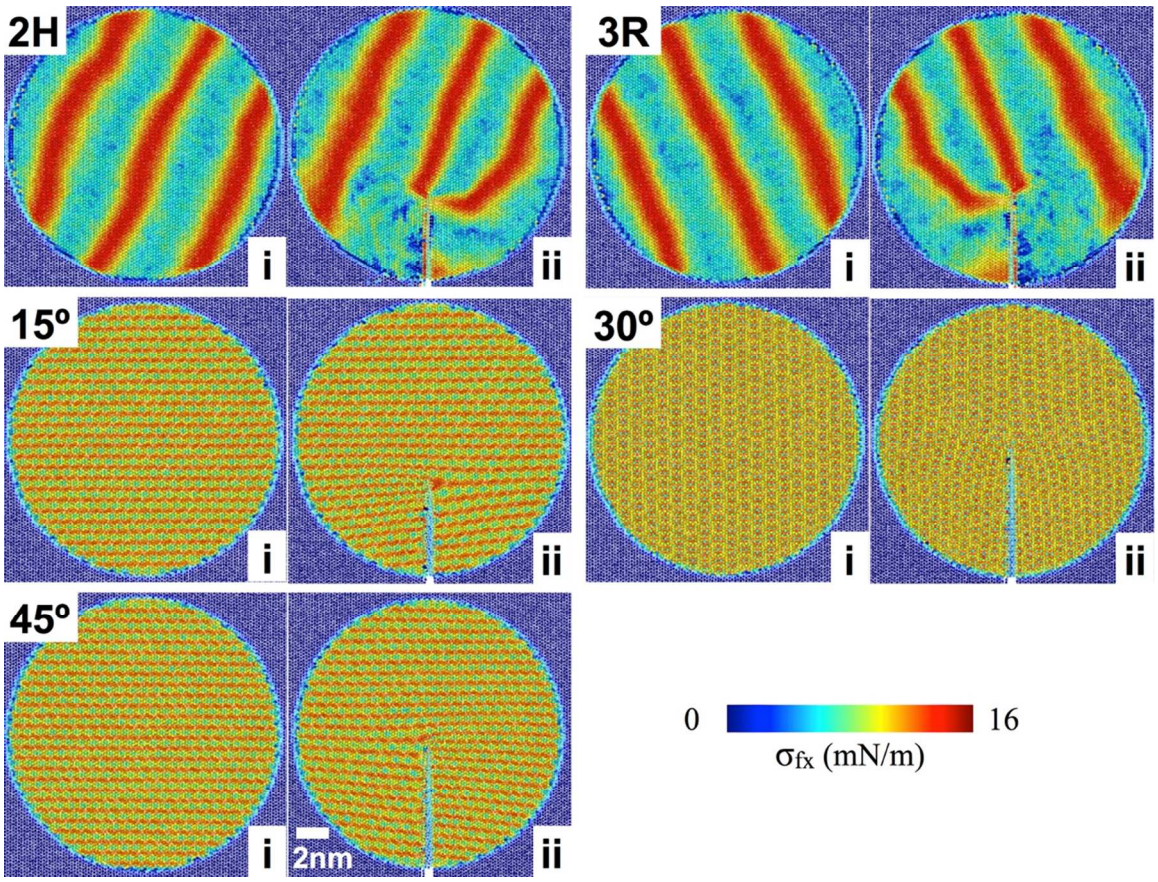

Figure S6. The interlocking friction distribution from vdW terms of sulfur atoms in the top and bottom layers with different stacks: 2H, 3R, 15º, 30º, and 0º. The sulfur atoms are colored according to their relative geometries estimated by the vdW terms (See Method). The two panels (i) and (ii) represent the distributions before and during the crack propagation, respectively. It can be assumed that the friction is applied to the opposite direction of the movement. Therefore, the distribution near the crack tip provides the crucial information to understand the crack behaviors. The two well ordered stacks (2H and 3R) show significantly different interaction before and during the propagation while the other stacks show weaker interaction. The 30º shows symmetric distribution while the 15º and 45º show asymmetric distribution, which results in the asymmetric moiré pattern during the propagation in Figure 3.

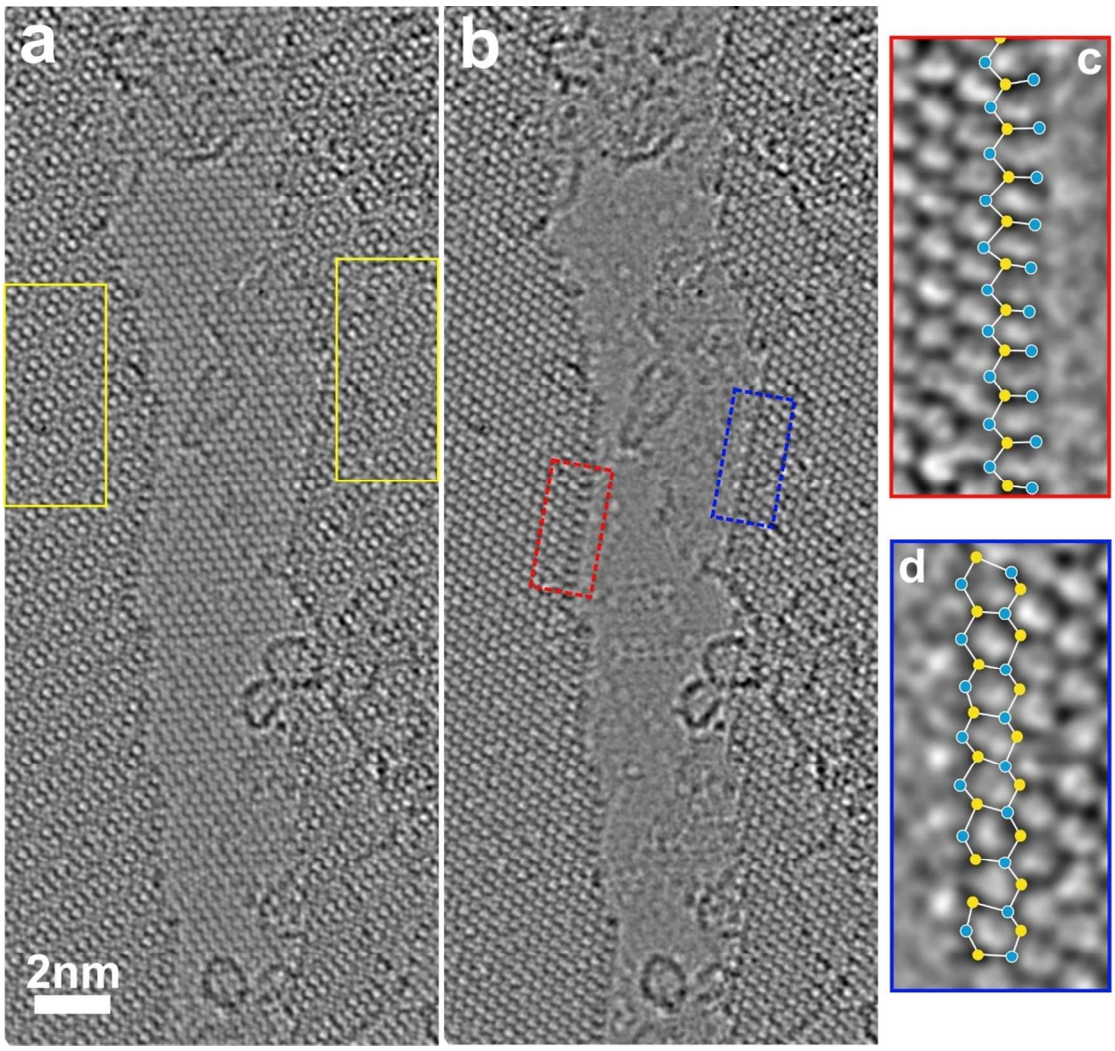

Figure S7. (**a**) AC-TEM image showing fractured edges in one layer of a turbostratic bilayer region. (**b**) Reconstructed AC-TEM image after filtering out the lattice contribution from the uncracked layer. (**c**) Zoom-in image of the edge structure in the dashed red box of panel **b** with atomic model overlaid. The blue and yellow spheres represent Mo and S atoms, respectively. (**d**) Zoom-in image of the edge structure in the dashed blue box of panel **b** with atomic model overlaid. The torn edges are along the zigzag lattice orientation, showing the same configuration as that in the monolayer MoS_2. This shows the ability to resolve the edge structure of the crack in bilayer MoS2 after filtering, and reveals similar edge structures to those we saw for monolayer MoS_2 cracks.

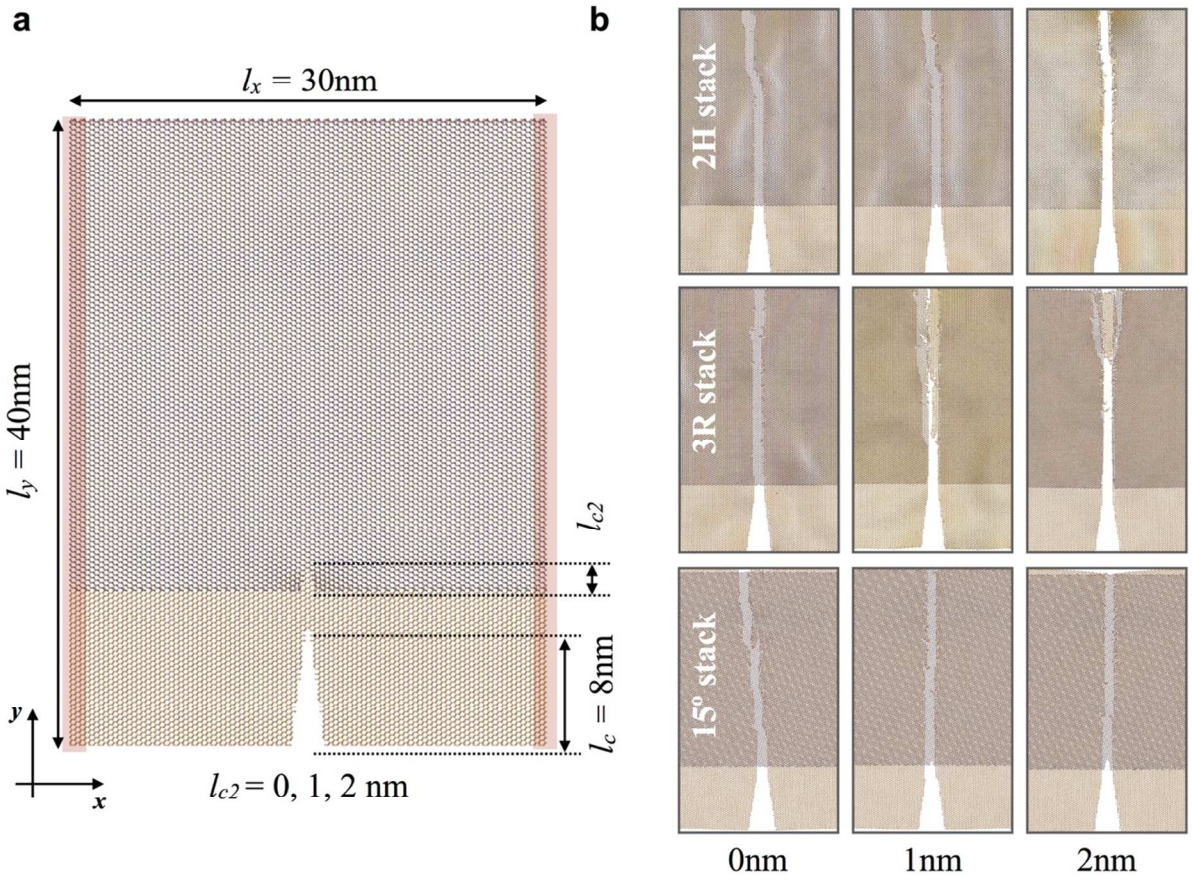

Figure S8. (**a**) Schematic figure for crack propagation in the bottom layer into semi-infinite bilayer regions with different lengths of flaws of the top layer (**b**) Results of crack propagations. The coherent fracture occurs with small flaws with 3R and 2H stacks but does not occur with15º turbostratically-stacked bilayer.

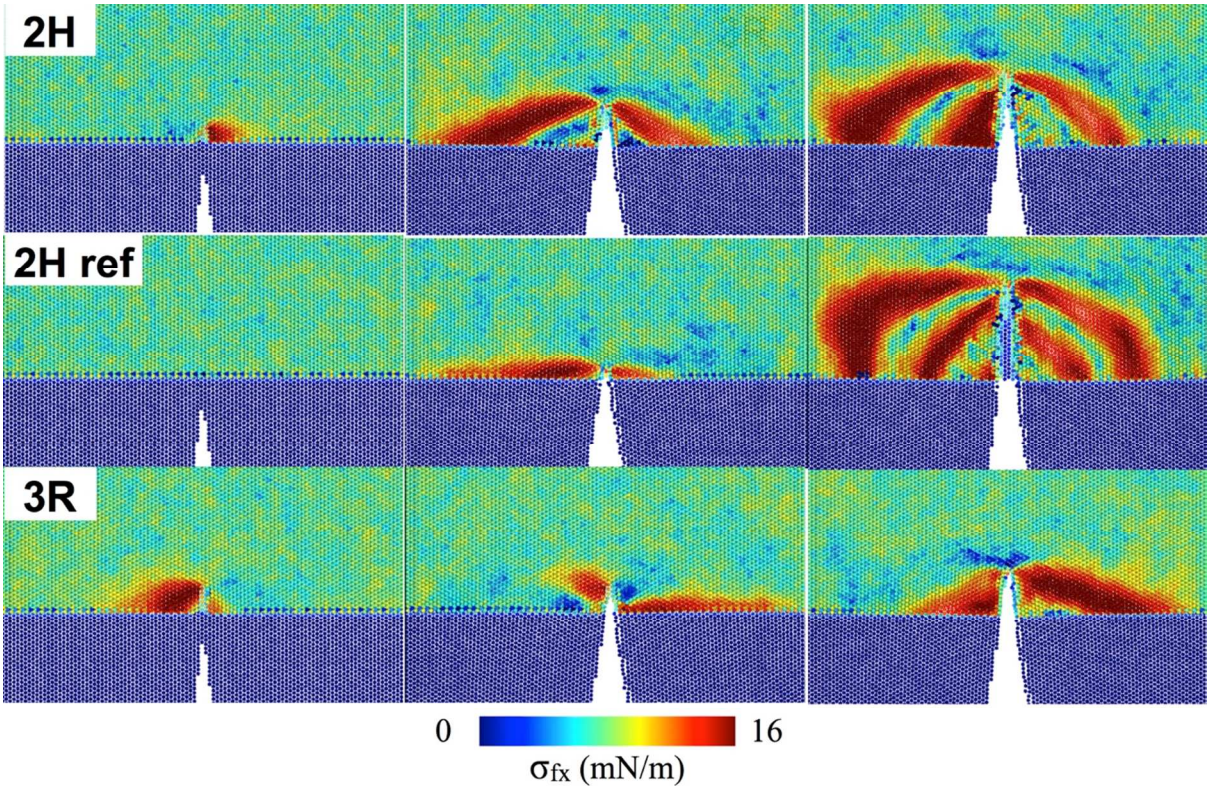

Figure S9. The interlocking friction distribution from vdW terms of the two sulfur atoms in the top and bottom layers to demonstrate the coherent fracture with different conditions. The sulfur atoms are colored according to their relative geometries estimated by the vdW terms (See method). The top layers of 2H and 3R have a small flaw of 2nm length on the crack path of the bottom layer. The highly activated frictions near the flaw are observed in both 2H and 3R while no activation of the friction without the small flaw in 2H ref. The initial interlocking friction causes effective tensile stress near the crack tip and coherent fracture occurs.

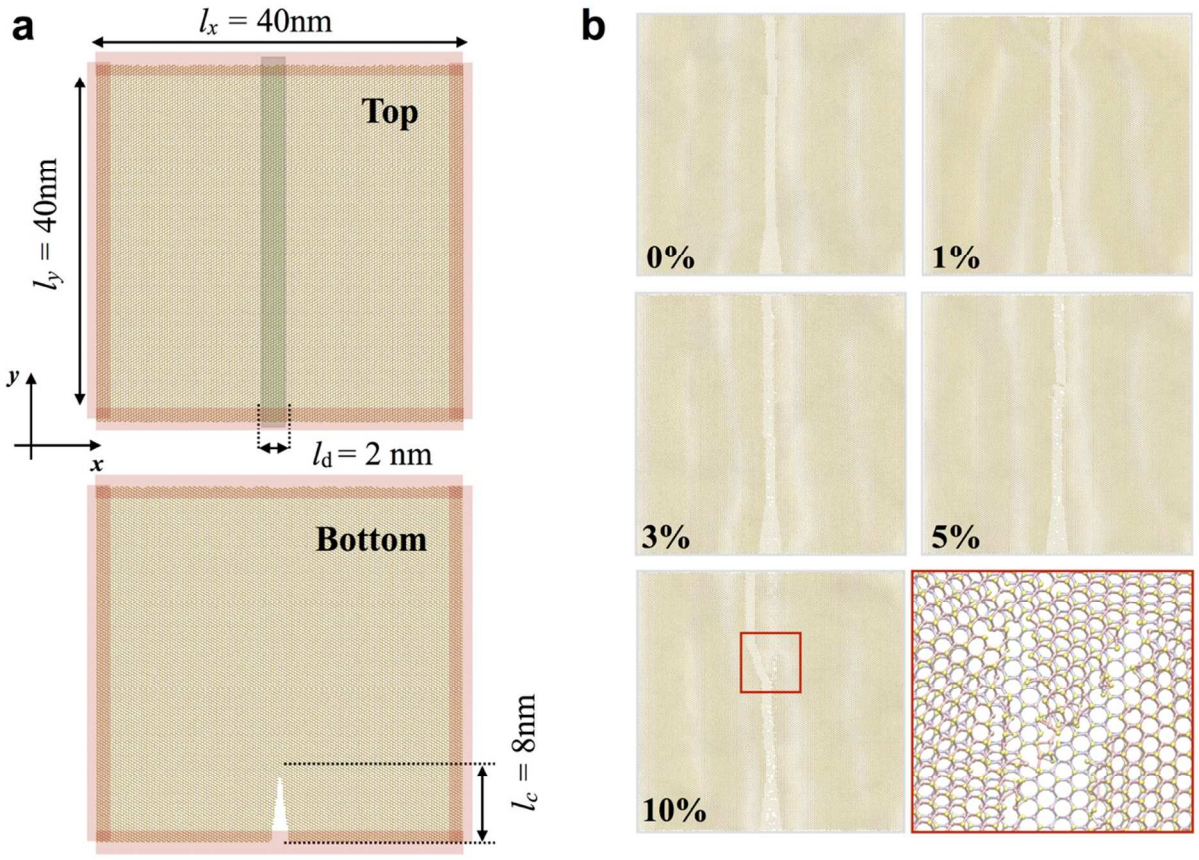

Figure S10. (**a**) Schematic figure for crack propagation in semi-infinite bilayer regions with different ratio of defects along the crack path. All edges are fixed with non-periodic boundary condition. The different ratios of defects are introduced in the top layer with a width l_d. (**b**) Results of crack propagations for different ratio from 0% to 10%. The crack is branched with 10% defects in the top layer. The coherent fracture occurs with 20% defect ratio.

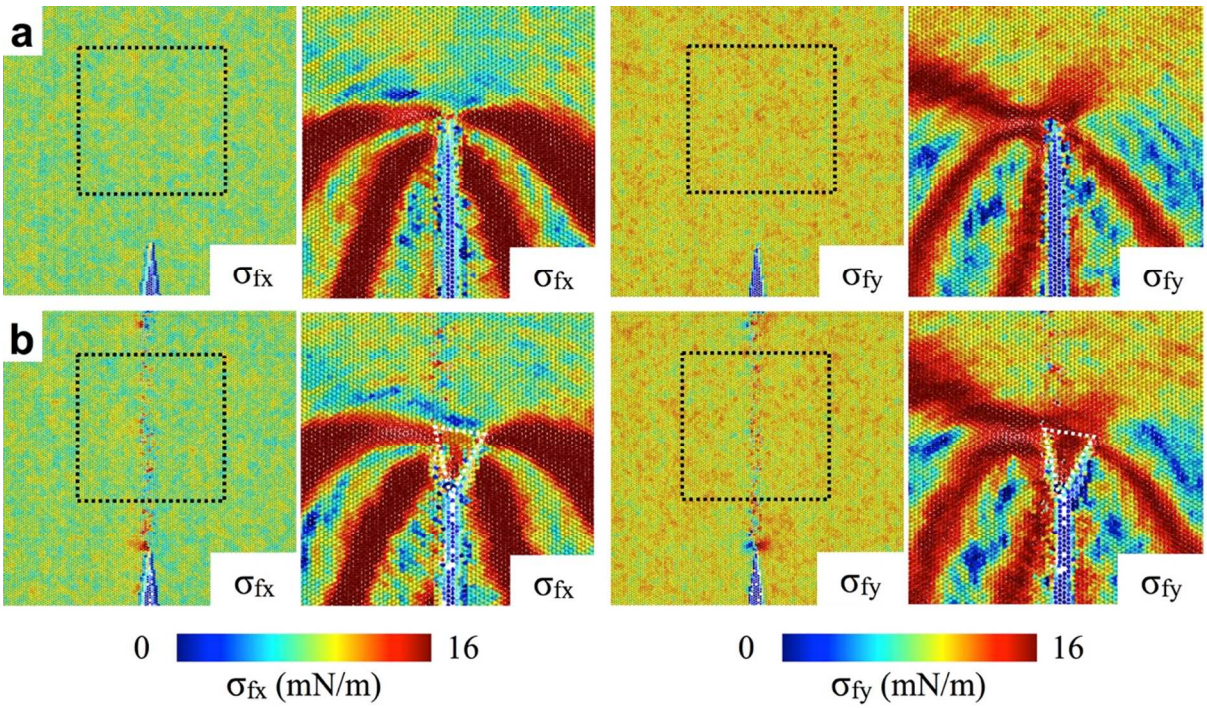

Figure S11. The interlocking friction distribution from vdW terms of sulfur atoms in the top and bottom layers without sulfur vacancies (**a**) and 10% sulfur vacancies (**b**) in the second layer. The sulfur atoms are colored according to their relative geometries estimated by the vdW terms (See method). There is asymmetric distribution of σ_{fy} in the x direction with 0%, which decides the branching direction when the crack branches. Highly activated friction is observed in the triangular island region.

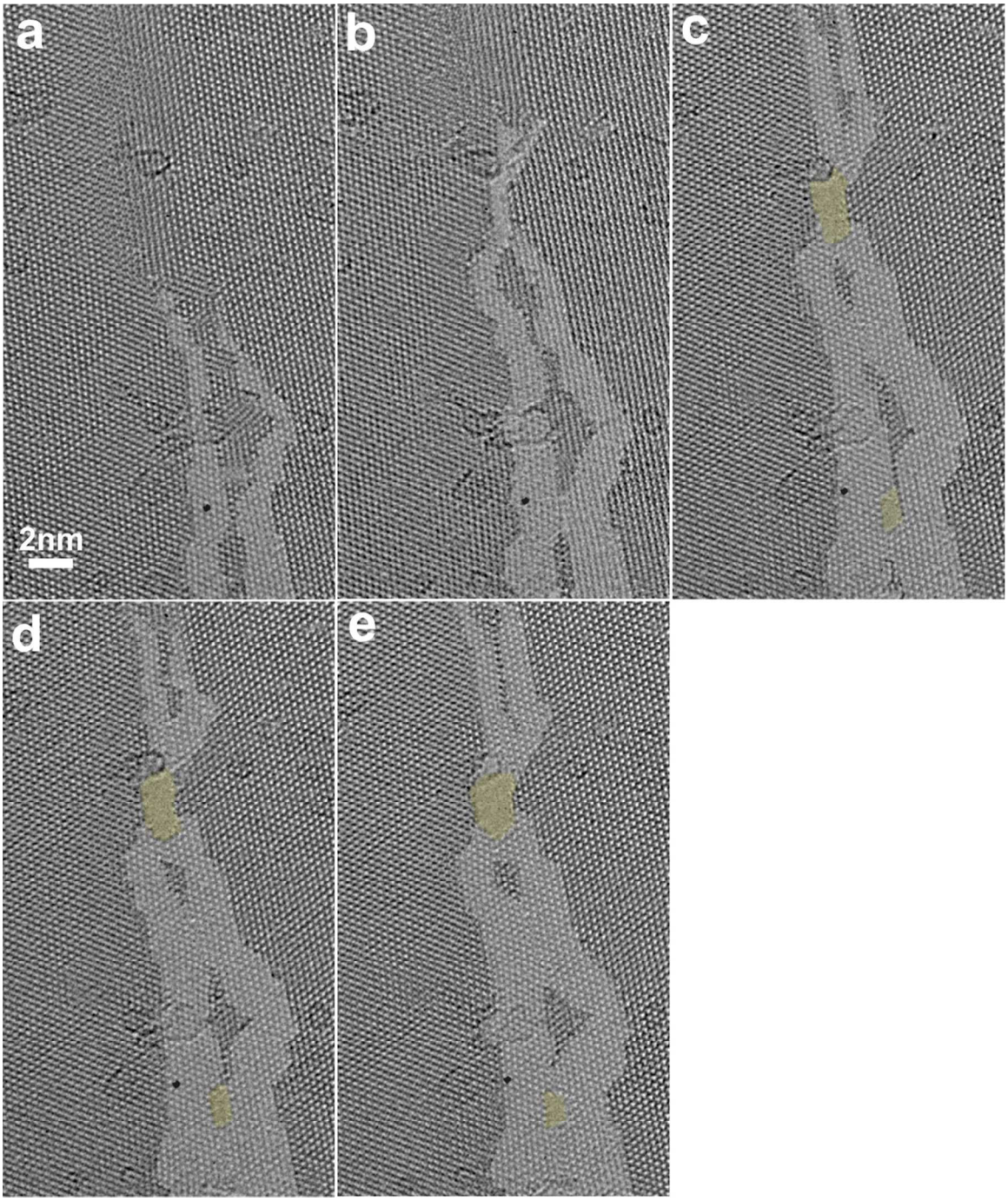

Figure S12. A time series of AC-TEM images showing branched crack propagation of this 2H-stacked bilayer region. Holes are formed during the fracture propagation, as marked by yellow regions. The remained bilayer islands originally show non 2H-stacked moiré patterns.

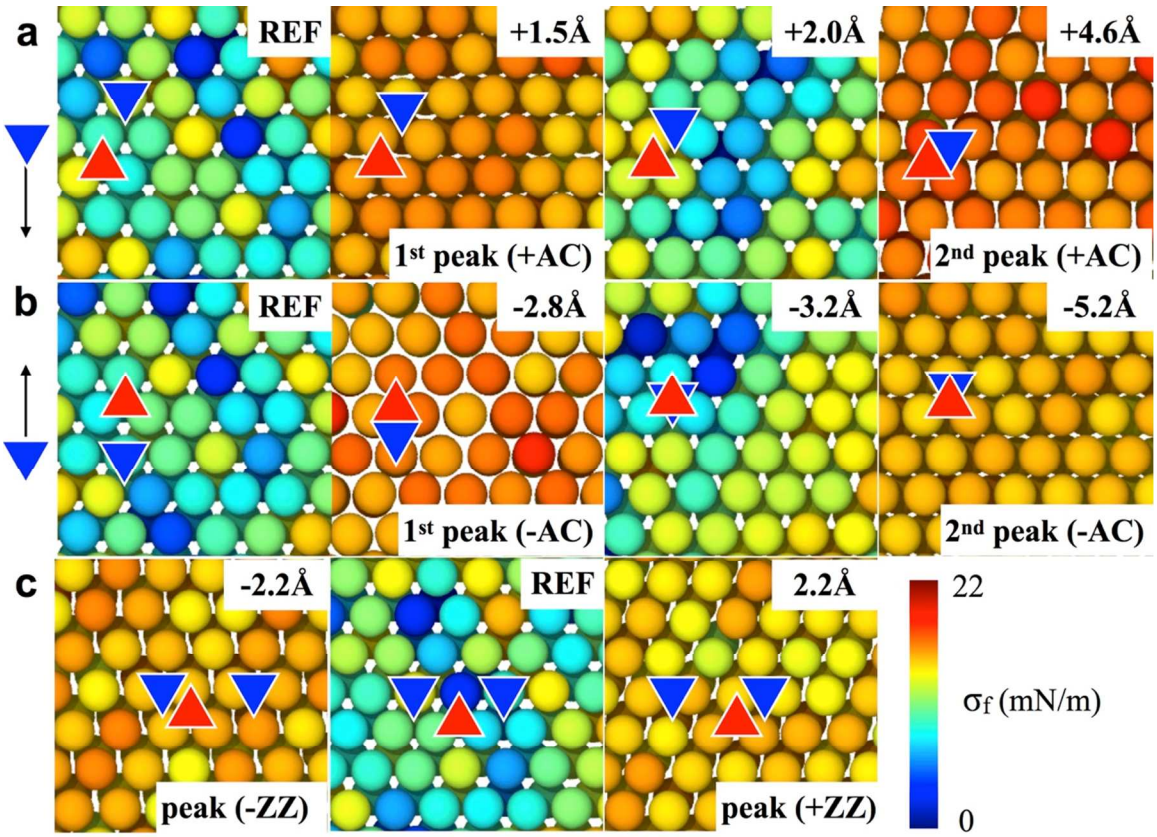

Figure S13. Snap shots of friction distribution of 2H stacks during the interlayer friction tests with four different loading directions. (**a**) positive and (**b**) negative armchair directions (+AC and –AC), and (**c**) the two zigzag directions (+ZZ and -ZZ) in Figure 2. The red and blue triangles represent the sulfur triangles in the top and bottom layers, respectively. The atomic stress from vdW terms between the bottom sulfurs in the top layer and the top sulfurs in the bottom layer, describe sulfurs' relative positions and therefore, it can be a good indicator for the interlocking friction (high friction distributions correspond to the friction peaks in Figure 2).